

Lab on a Chip

Accepted Manuscript



This is an *Accepted Manuscript*, which has been through the Royal Society of Chemistry peer review process and has been accepted for publication.

Accepted Manuscripts are published online shortly after acceptance, before technical editing, formatting and proof reading. Using this free service, authors can make their results available to the community, in citable form, before we publish the edited article. We will replace this *Accepted Manuscript* with the edited and formatted *Advance Article* as soon as it is available.

You can find more information about *Accepted Manuscripts* in the [Information for Authors](#).

Please note that technical editing may introduce minor changes to the text and/or graphics, which may alter content. The journal's standard [Terms & Conditions](#) and the [Ethical guidelines](#) still apply. In no event shall the Royal Society of Chemistry be held responsible for any errors or omissions in this *Accepted Manuscript* or any consequences arising from the use of any information it contains.

Droplet actuation in an electrified microfluidic network

Jonathan D. Wehking, and Ranganathan Kumar*

Received Xth XXXXXXXXXXXX 20XX, Accepted Xth XXXXXXXXXXXX 20XX

First published on the web Xth XXXXXXXXXXXX 200X

DOI: 10.1039/b000000x

This work demonstrates that liquid droplet emulsions in a microchannel can be deformed, decelerated and/or pinned by applying a suitable electrical potential. By concentrating a potential gradient at the corners, we show that different droplets can be passively binned by size and on demand in a branched microfluidic device. The deformation, deceleration, squeezing and release of droplets in a three-dimensional numerical simulation are qualitatively verified by experiments in a PDMS microfluidic device. The forces required for pinning or binning a droplet provide a delicate balance between hydrodynamics and the electric field, and are obtained using appropriate non-dimensional parameters.

1 Introduction

Electric fields offer a means of non-intrusive manipulation and control over flowing liquid droplet emulsions, and offer technological leaps in heat exchanger design, ink-jet printing, optical emulsification technologies, drug delivery, and high-throughput microscale assays^{1–13}. Sato *et al.*¹⁴ investigated the effects of electrification on co-flowing immiscible fluids, and demonstrated synchronous droplet formation with electrified laminar jet surface wave frequencies. Fernandez and Tryggvason¹⁵ simulated droplet motion and behavior in both stationary and simple Poiseuille flow for several droplet/medium fluid combinations, and observed predictable droplet migration depending on the deformed shape (prolate/oblate). Singh and Aubry¹⁶ studied droplets flowing over a two electrode configuration where both the positive and negative electrodes were located on the same channel wall, and positioned very close to each other such that droplets were captured and coalesced. Krupenkin and Taylor¹⁷ utilized reverse electrowetting (REWOD) to extract electrical energy from droplets located in the soles of shoes, mechanically deformed by walking or running. Over a large number of droplets and steps, power densities up to 10^3 W m^{-2} were harvested, enough to power a typical electronic mobile device. Electrocoalescence was utilized by Abate *et al.*¹⁸ to develop a high-throughput method of adding reagents to droplet microreactors using picoinjectors. Agresti *et al.*¹⁹ was able to dielectrophoretically sort droplets according to fluorinated enzyme variants on the surfaces of yeast cells by presetting a fluorescence intensity threshold. Recent studies have also characterized droplet deformation due to the presence of a transverse alternating electric field²⁰, and direct current (DC) electrowetting^{21–23}.

University of Central Florida, Orlando, Florida, 32816, USA. Fax: XX XXXX XXXX; Tel: XX XXXX XXXX; E-mail: Ranganathan.Kumar@ucf.edu

In a prior work (Wehking *et al.*²⁴), we conducted a proof-of-concept two-dimensional numerical simulation of electrically induced droplet deformation following the leaky dielectric model. The droplet pinning was characterized using the electric Euler number, and manipulated in different directions within a T-junction by applying steep gradients of electrical potential at the T-junction corners. In this work, we simulate full three-dimensional microfluidic geometries to allow for comparison to experiments. In addition, we broaden our analysis to include the magnitudes of all forces present during droplet deceleration and pinning, rather than limit the analysis only to inertial and electric forces. By fully understanding the fundamental force balance during droplet deceleration and pinning, we are able to bin droplets by size in a branched microfluidic network.

2 Formulation

2.1 Governing Equations and Numerical Model

Electrohydrodynamics provides the necessary forces to greatly influence the behavior of flowing liquid droplet emulsions. Equations governing the fluid mechanics are the incompressible continuity $\nabla \cdot (\rho \mathbf{v}) = 0$ and momentum equations (equation 1).

$$\frac{\partial(\rho \mathbf{v})}{\partial t} + \rho(\mathbf{v} \cdot \nabla) \mathbf{v} = \nabla \cdot [-p \mathbf{I} + \mu(\nabla \mathbf{v} + (\nabla \mathbf{v})^T) + \sigma^M] + \gamma \kappa \delta \hat{\mathbf{n}} \quad (1)$$

The velocity field, pressure, time, fluid density, and viscosity are denoted by \mathbf{v} , p , t , ρ and μ respectively. The interfacial tension between phases is γ , κ is the interface curvature, δ is the Dirac delta function, and $\hat{\mathbf{n}}$ refers to the normal direction

with respect to the droplet surface. \mathbf{I} is the identity matrix. The Maxwell stress tensor (σ^M) is shown in equation 2⁴.

$$\sigma^M = \varepsilon \varepsilon_0 \mathbf{E} \mathbf{E} - \frac{1}{2} \varepsilon \varepsilon_0 \left[1 - \frac{\rho}{\varepsilon} \left(\frac{\partial \varepsilon}{\partial \rho} \right) \right] (\mathbf{E} \cdot \mathbf{E}) \mathbf{I} \quad (2)$$

The fluid relative permittivity and electric field are given by ε and \mathbf{E} , respectively, and the vacuum permittivity is $\varepsilon_0 = 8.854 \times 10^{-12} \text{ F/m}$. The second term in the brackets of equation 2 is the electrostriction term, and can be neglected since the fluids are considered incompressible. Equations 1 and 2 can be normalized using the following dimensionless quantities: $t^* = t/w_c v_c$, $\mathbf{v}^* = \mathbf{v}/v_c$, $p^* = p/\rho_c v_c^2$, $\mathbf{E}^* = \mathbf{E}/E_0$, $\kappa^* = \kappa/w_c$, $\delta^* = \delta/w_c$, $\rho^* = \rho/\rho_c$, $\mu^* = \mu/\mu_c$, $\varepsilon^* = \varepsilon/\varepsilon_c$. The channel width, average velocity, density, viscosity, and relative permittivity are denoted by w_c , v_c , ρ_c , μ_c and ε_c , respectively, where the subscript c refers to the continuous (or suspending) fluid. E_0 is a characteristic electric field, and will be defined later. When these terms are applied to equation 1, the resulting dimensionless momentum equation becomes (with the * superscript removed for clarity):

$$\rho \frac{\partial \mathbf{v}}{\partial t} + \rho (\mathbf{v} \cdot \nabla) \mathbf{v} = -\nabla p + Re^{-1} \nabla \cdot \mu (\nabla \mathbf{v} + (\nabla \mathbf{v})^T) + Eu_e^{-1} \nabla \cdot \sigma^M + We^{-1} \kappa \delta \hat{\mathbf{n}} \quad (3)$$

This normalized momentum equation still contains physical properties such as ρ (density) and μ (viscosity) because the multiphase system has been reduced to singular governing equations using the level set method²⁵. The level set equation then tracks each of the phases in the domain using the variable ϕ , which is based on the volume fraction and takes on values between 0 and 1. The physical properties are then defined as $\rho = \rho_c + (\rho_d - \rho_c)\phi$ (using density as an example), where ρ_c and ρ_d represent the true densities of the continuous and droplet phases, respectively. Therefore, when solving the problem in the continuous fluid, $\phi = 0$, which will make $\rho = \rho_c$, and when solving the problem within the droplet, $\phi = 1$, and $\rho = \rho_d$. At the interface, ϕ takes on values between 0 and 1, and will utilize the corresponding “smeared” values between ρ_c and ρ_d . This is identically used for the fluid viscosity, relative permittivity, and electrical conductivity (σ , used later). The dimensionless numbers Re , Eu_e , and We are the Reynolds number ($Re = \rho_c v_c w_c / \mu_c$), electric Euler number ($Eu_e = \rho_c v_c^2 / E_0^2 \varepsilon_0 \varepsilon_c$), and Weber number ($We = \rho_c v_c^2 w_c / \gamma$), respectively. The equation governing the potential distribution is the conservation of charge $\nabla \cdot (\sigma \mathbf{E}) = 0$, following the leaky dielectric model since the electric field is assumed to develop much faster than the flow field. The electric forces influence the fluid behavior through the Maxwell stress tensor (σ^M) in equation 3. A three-dimensional finite element model was implemented in COMSOL Multiphysics,

with a mesh consisting of $\approx 13,400$ tetrahedral elements after removing half of the domain due to symmetry. Linear element discretization was used for velocity and pressure variables, and a quadratic discretization for the electrical potential. The formulation, normalization and numerical scheme follows Wehking *et al.*²⁴.

The three-dimensional numerical model (*qualitatively* validated by experiments later) studies the behavior of droplets in a microchannel when a smoothed step function of electrical potential is applied along the lower channel wall. The step profile is shown graphically using a red dashed line in figure 1, and spans potential values (i.e. voltage) from $V = V_0$ to $V = 0$. The step function boundary condition is chosen to match the experimental microfluidic device with indium electrodes implanted using microsolidics (shown later)²⁶. The upper channel wall is left grounded ($V_0 = 0$, same in experiments) in order to isolate electrohydrodynamic phenomena attributed to the step profile at the lower wall. All remaining boundaries (including the inlet, outlet, and left over channel walls) are fixed at zero potential gradient. Hydrodynamic boundary conditions consist of a fully developed constant flow rate at the inlet, zero pressure with no viscous stress at the outlet, and a fixed hydrophobic contact angle at all microchannel walls. This system results in droplet deceleration and pinning along the lower channel wall where the electrical potential smoothed step boundary condition is applied.

A force diagram depicting “unconfined” and “confined” droplets of two different diameters is shown in figure 1. A droplet is “unconfined” when its surfaces do not contact the microchannel walls, and the droplet remains spherical (upper diagram). A droplet is “confined” when its surfaces contact the microchannel walls, impacting its overall shape (lower diagram). Figure 1 depicts the droplet shape of both “unconfined” and “confined” droplets immediately upstream of the pinning site, then at the pinning site. The forces present on the droplet are divided into two categories: hydrodynamic forces (inertial, viscous, pressure, and interfacial forces), and electric forces, with arrows representing their respective directions in the system.

2.2 Experimental Validation of Numerical Results

An experiment was performed using a PDMS microfluidic device with indium electrodes in a similar configuration to the pinning simulations, and compared to droplet behavior observed in simulations (refer to figure 2). Since the electrodes are generated using microsolidics, they can be placed closer to the flowing droplets. However, the bulk PDMS material above and below the electrodes damp the electric field. In addition, the experimental electrodes are the same depth as the microchannels themselves ($50 \mu\text{m}$). In the experiment, V_0 at the channel walls is an order of magnitude larger than V_0 used

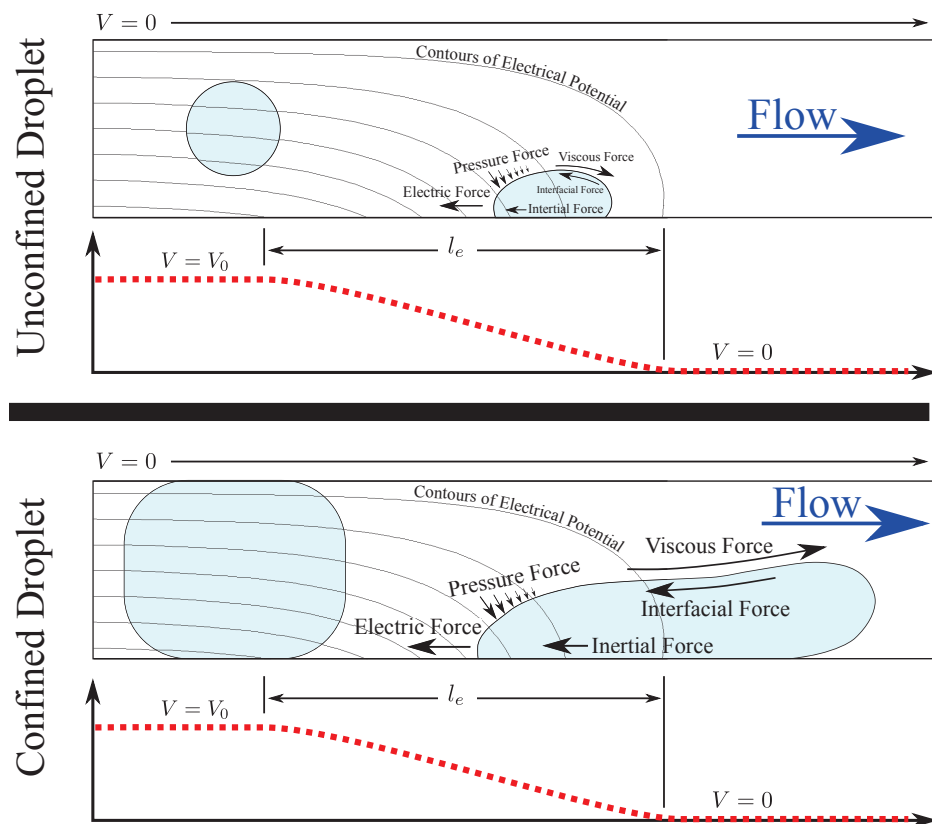


Fig. 1 Force diagram on unconfined and confined droplets, with boundary conditions used for electrical potential. A smoothed step potential gradient is used on bottom boundary, and zero potential is used on top boundary (grounded). Contours represent equipotential lines, and are shown for the continuous fluid only for clarity (droplets superimposed on top). For the full potential distribution through the system, refer to figure 2 (“Numerical”) and figure 4.

in the simulations for similar droplet sizes to make up for the damping and dielectric leak into the PDMS. Therefore, quantitative comparison between simulation and experiment is difficult due to the difference in the electric potential along the channel wall. A completely leaky dielectric or perfect dielectric analysis on water or silicone oil would show that the experimental applied voltage needs to be between five to ten times the actual voltage realized at the point of interest to account for this damping and charge leak. The following analysis on relaxation times would show that, between water and silicone oil, conflicting assumptions on the governing equations would have to be made.

Noting that the subscripts c and d indicate continuous and dispersed phases, the electric relaxation time is quantified by $t^E = \epsilon/\sigma$, which gives $t_c^E \approx 23s$ for silicone oil and $t_d^E \approx 128\mu s$ for deionized water. The hydrodynamic relaxation time is given by $t^H = \rho w_c h/\mu$, which gives $t_c^H \approx 0.25ms$ for silicone oil and $t_d^H \approx 5ms$ for deionized water. When comparing the timescales for deionized water (subscript d), $t_d^E \ll t_d^H$,

meaning the electric field develops much quicker than the flow field and the charge accumulating at the droplet surface can be assumed steady (or instantaneously developed) at each time step. This assumption of a leaky dielectric model is used in the current simulations. However, when comparing timescales for silicone oil (subscript c), $t_c^E \gg t_c^H$, meaning the electric field develops much slower than the flow field and the charge accumulating at the droplet surface is nearly non-existent at each time step. In this case, the material can be treated as a perfect dielectric. This conflict in theoretical assumptions, along with the presence of additional PDMS above and below the electrodes can explain the disparity in applied V_0 between experiments and simulations.

Therefore, the experimental verification was done at 3500V, which is seven times the numerical voltage. This value is reasonable based on running a simulation on only water or oil. Since voltage is damped in a system comprised of both silicone oil (perfect dielectric material), and water (leaky dielectric material), the multiplication factor of seven is chosen

Table 1 Physical properties of materials tested.

Liquid (-)	Density (kg/m^3)	Dynamic Viscosity ($Pa \cdot s$)	Electrical Conductivity (S/m)	Relative Permittivity (-)
DI Water	1000	1×10^{-3}	5.5×10^{-6}	80
20cSt Oil	950	19×10^{-3}	8.3×10^{-13}	2.2

since the model chosen is leaky dielectric. The experimental voltage of 3500V allows excellent prediction of droplet behavior in the three regions. Upstream of the pinning site, the droplet deforms into a prolate spheroid due to the electric field developing across the channel width and the fluids' material properties. The pinning site causes droplet deceleration, and pinning if the electric force is strong enough. If the droplet is not pinned, then downstream of the pinning site the droplet is not electrified, and returns to its nominal shape. These regions are highlighted in figure 2 for experimental and three-dimensional simulations. Prolate droplets are deformed parallel to the electric field (elongated vertically in our simulations), and oblate droplets are deformed perpendicular to the electric field²⁴. Thus, despite any quantitative discrepancies between experiments and simulations in electrode placement, applied voltage and drop size, electric field induced deceleration, squeezing, pinning and release of the droplet is evident.

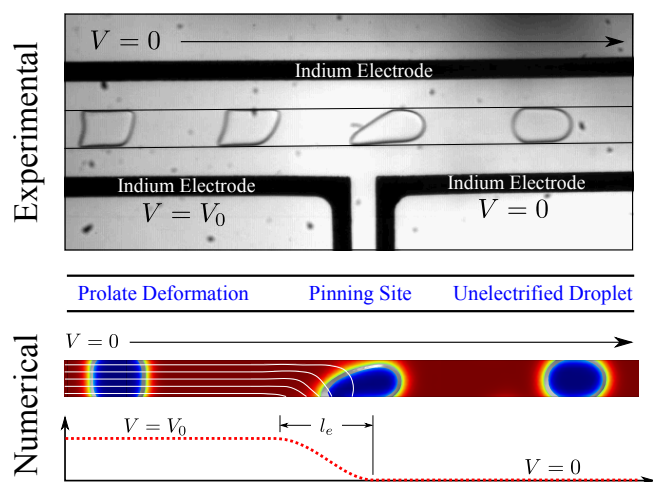


Fig. 2 Qualitative comparison between experiments and three-dimensional numerical droplets. The continuous fluid is silicone oil and the dispersed fluid is deionized water (see table 1 for material properties), with $Q_c = 200 \mu L/hr$, $Re = 0.04$ and $V_0 = 3500V$. The white lines in the simulation are equipotential lines with $V_0 = 500V$.

2.3 Order of Magnitude Analysis

Droplet pinning can be characterized using a fundamental order of magnitude force balance. The electric force contains non-uniform horizontal and vertical components as shown by the contours of electrical potential (figure 1). The largest component of the electric force, the dielectric force, is acting everywhere normal to the affected droplet surface, and always from the fluid with higher relative permittivity on the fluid with lower relative permittivity. It is strongest at the bottom channel wall, and the magnitude of this force is estimated as

$$F_{Electric} \sim E_0^2 \epsilon_c \epsilon_0 (hl_e) \sim O(1) \mu N \quad (4)$$

The electric force on the droplet is due to the presence of an electric field, and is estimated by the gradient of the potential step at the lower channel wall, $E_0 = (V_0 - 0)/l_e$, where V_0 is the applied potential, and l_e is the distance over which the potential decays to $V = 0$. ϵ_c and ϵ_0 are the continuous phase relative permittivity and the vacuum permittivity, respectively, and h is the channel height (dimension perpendicular to the page). The product (hl_e) refers to the area over which the electric stress is applied along the lower channel wall to obtain the effective electric force, which is acting in the direction opposite of the flow. It is worth noting that the electric force formulated in equation 4 does not depend on the drop size, since this force only acts on a transition between relative permittivities at the droplet's surface (approximated by the relative permittivity of the continuous phase, ϵ_c , since there is at least double the amount of continuous phase than dispersed phase in the system).

The hydrodynamic forces are divided into three types (volumetric, surface area, and edge forces) depending on how they act on the drop size. The expressions for these forces are left in terms of the droplet volume, surface area, and arc length, respectively, which are all dependent on the drop diameter. This is to keep the order of magnitude force balance independent of the drop size (and the confined/unconfined distinction). The droplet inertial force depends on the droplet mass and acceleration, and is estimated as

$$F_{Inertial} \sim \frac{\rho_d u_{ave}^2}{l_e} \left[\frac{4}{3} \pi \left(\frac{d}{2} \right)^3 \right] \sim O(1.19 \times 10^9 d^3) \mu N \quad (5)$$

where d is the *undeformed* droplet diameter. Note that the expression in the rightmost brackets is the undeformed droplet volume. The acceleration scale is estimated by a characteristic velocity (u_{ref}) over an interval of time ($t \approx l_{ref}/u_{ref}$). The characteristic velocity is chosen to be the average inlet velocity of the system $u_{ave} = Q_c/(w_c h)$ (Q_c is the inlet flow rate) and the reference length is distance over which the droplet would be brought to rest ($\approx l_e$) so the acceleration is proportional to u_{ave}^2/l_e . The droplet inertial force is always opposing the direction of the droplet acceleration for a pinned droplet.

The surface area forces on the droplet are of two types: viscous shear and upstream pressure. The viscous shearing force is the tugging force of the continuous flow past the stationary (or decelerating) droplet, and is estimated as

$$F_{Viscous} \sim \frac{\mu_c u_{gap}}{w_{gap}} \frac{1}{2} \left[4\pi \left(\frac{d}{2} \right)^2 \right] \sim O(1.46 \times 10^8 d^2) \mu N \quad (6)$$

where the expression in the rightmost brackets is the undeformed droplet surface area. The viscous shearing force depends on the continuous phase viscosity (μ_c), the rate of shear strain, and the exposed droplet surface area $[4\pi(d/2)^2/2]$. As the droplet is pinned to the lower channel wall, it acts as an obstruction, causing the continuous fluid flow to pass through the narrow gap created above the droplet. Due to this blockage of the continuous fluid, the surface area effected by viscous shear is not the entire surface area of the droplet, and is instead estimated to be half of the undeformed droplet surface area. The shear rate ($\partial u/\partial y$) is estimated by the quotient of the velocity through the gap and the gap width (u_{gap}/w_{gap}). The gap width (w_{gap}) will also depend on the drop diameter, but the dependency on the diameter is kept to the effective surface area for this analysis. To obtain the order of magnitude in equation 6, $w_{gap} \approx w_c/4$, and $u_{gap} \approx Q_c/(w_{gap} h)$.

The pressure forces are generated by the pinned droplet blocking the continuous fluid flow. This larger upstream pressure creates a squeezing force over the exposed droplet surface area, and is estimated using the Hagen-Poiseuille approximation through the gap.

$$F_{Pressure} \sim \frac{\mu_c w_c Q_c}{w_{gap}^3 h} \frac{1}{2} \left[4\pi \left(\frac{d}{2} \right)^2 \right] \sim O(5.84 \times 10^8 d^2) \mu N \quad (7)$$

where exposed droplet surface area is the same used for approximating the viscous force $[4\pi(d/2)^2/2]$. The effective gap length is estimated to be w_c , and will also depend on the droplet size, but as with the viscous forces, the dependency on the diameter is kept to the effective surface area for this analysis. To obtain the order of magnitude result in equation 7, $w_{gap} \approx w_c/4$.

The remaining force affecting pinning is the droplet surface tension. The surface tension force acts as a restoring force trying to keep the droplet intact, and acts tangentially to the droplet boundary. This force is estimated as

$$F_{Interfacial} \sim \gamma \frac{1}{2} (\pi d) \sim O(7.07 \times 10^4 d) \mu N \quad (8)$$

where γ is the surface tension coefficient for the fluid pair, and d is the undeformed droplet diameter. Like the surface area forces, this force acts over the exposed half of the droplet once it is pinned, but is only affected by the droplet circumference ($\pi d/2$).

If the magnitudes of all the forces are summed (according to the sign convention in figure 1) at the point where a droplet is about to be pinned, an order of magnitude force balance is obtained. Separating all the electric forces from the hydrodynamic forces, the result is shown in equation 9a. If the electric force is divided through the entire equation, a *dimensionless* force balance is achieved, thus illuminating a critical combination of force ratios necessary for pinning with dependencies on the drop diameter. This is shown in equation 9b.

$$F_{Electric} \sim -F_{Inertial} + F_{Viscous} + F_{Pressure} - F_{Interfacial} \quad (9a)$$

$$1 \sim -Eu_e + Ma + Ps - Ca_e^{-1} \quad (9b)$$

Eu_e is the electric Euler number (ratio of inertial to electric forces) which reduces to $Eu_e = (\rho_d u_{ave}^2 \pi / 6h V_0^2 \epsilon_c \epsilon_0) d^3$; Ma is the Mason number (ratio of viscous to electric forces) which reduces to $Ma = (\mu_c u_{gap} l_e \pi / 2hw_{gap} V_0^2 \epsilon_c \epsilon_0) d^2$; and Ca_e^{-1} is the inverse of the electric capillary number (ratio of electric to interfacial forces) which reduces to $Ca_e^{-1} = (\sigma l_e \pi / 2h V_0^2 \epsilon_c \epsilon_0) d$. All dimensionless quantities are common in electrohydrodynamics except for Ps , which is not any dimensionless number known at this time, but represents the ratio of pressure to electric forces and reduces to $Ps = (\mu_c w_c Q_c l_e \pi / 2w_{gap}^3 h^2 V_0^2 \epsilon_c \epsilon_0) d^2$. This force balance is offered solely as an order of magnitude study in order to help characterize droplet pinning.

3 Results and Discussion

3.1 Droplet Pinning

The electric force required for pinning a droplet (six cases in the *undeformed* diameter range of $41.7 \mu m$ to $116.7 \mu m$) was simulated in a silicone oil / deionized water system (table 1). Though the true conductivity value is listed for each material in table 1, it is assumed the system becomes insensitive to the true conductivity ratio when it exceeds a value of $\sigma_d/\sigma_c \geq 100$ (according to studies by Feng and Scott⁸). This condition is easily satisfied in our system, and helps prevent numerical divergence due to large physical property gradients at the droplet

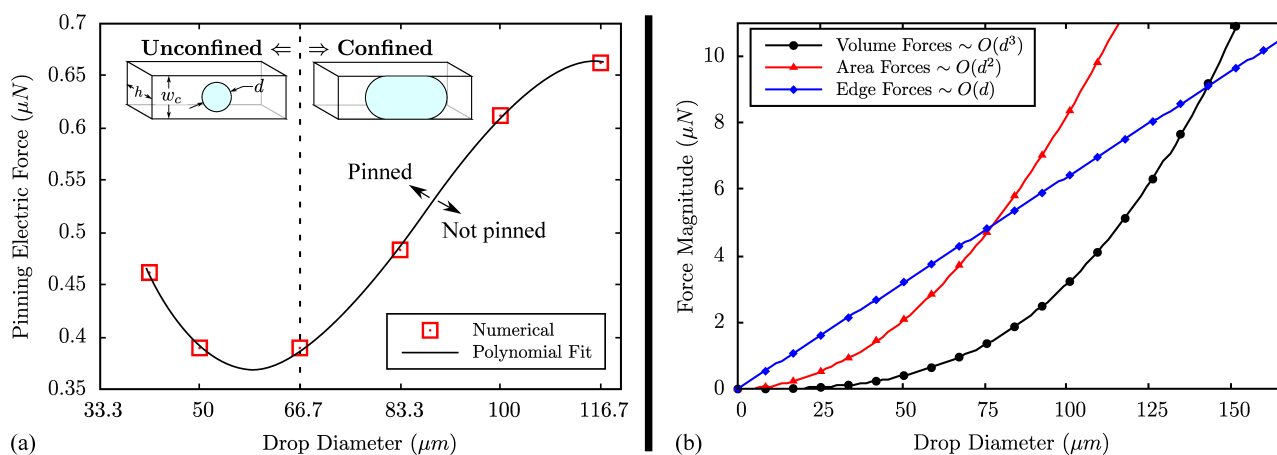


Fig. 3 (a) Three-dimensional electric pinning force dependency on dimensionless drop diameter. Polynomial fit is $F_E = O(\mu\text{N}) = -3.136 \times 10^{12}d^3 + 8.195 \times 10^8d^2 - 6.369 \times 10^4d + 1.919$, with $R^2 = 0.999$. (b) Individual magnitudes of polynomial fit in shown in (a). Note that $d = O(m)$ when using the curve fit.

boundaries. The dimensions of the microchannel (see figure 3a) are $w_c = 100\mu\text{m}$, $h = 50\mu\text{m}$, with the flow rate fixed at $Q_c = 550\mu\text{L/hr}$ ($Re = 0.1$). For the smoothed step in electrical potential at the pinning site, $l_e \approx 390\mu\text{m}$ (see figure 1). The applied electrical potential (V_0) was then adjusted until pinning occurred for each of the six different droplet diameters. Each data point required about twenty simulations to resolve the exact value for V_0 to within a 1.2% uncertainty. Figure 3a illustrates the results of the pinning force required for each droplet diameter simulated. When the electric force decreases below the data point plotted for each drop diameter, the droplet is no longer pinned, but may exhibit some deceleration and deformation at the pinning site before continuing downstream. When the electric force increases above each data point, the droplet is still pinned, but exhibits erratic behavior when the electric force is excessive.

The trend of the pinning force for each of the droplet sizes exhibits features that can be supported through physical explanations. As the droplet size (and undeformed drop diameter d) increases, the force necessary for pinning will increase due to the added droplet surface area on which viscous shear and pressure forces will act. However, there exists a minimum pinning force, located between $50\mu\text{m} < d < 66.7\mu\text{m}$. Then, as the drop diameter decreases further, the electric force required for pinning increases once again. When the droplet diameter decreases below $d = 50\mu\text{m}$, the droplet boundary is far enough away from the channel walls to be affected by the steep gradient in electrical potential at the channel boundary as it passes the pinning site. This is because the electric field strength weakens as it progresses into the continuous channel and polarizes the continuous fluid. Therefore, this smaller droplet receives a fraction of the original strength of the electrical potential step, and thus requires a greater electric force to draw

the droplet down to the channel wall in order to be pinned. All droplets were positioned at the center of the continuous channel before traveling to the pinning site. If the droplet were to enter the pinning site flowing along the channel boundary that contained the steep potential gradient, the electric pinning force would be greatly reduced. The minimum pinning force, located between $50\mu\text{m} < d < 66.7\mu\text{m}$, is when the droplet size is large enough to almost start making contact with the channel walls. Having a droplet boundary already flowing near the channel wall containing the steep gradient allowed for pinning to occur without the added effort of first pulling the droplet out of the continuous flow and toward the pinning site. This same droplet is also small enough to keep the surface area forces low (pressure and viscous shear) so that pinning can occur. This droplet diameter range represents an optimized balance of electric and hydrodynamic forces, or “sweet spot,” where a minimum pinning force can be achieved for this flow system.

In order to understand the trends from the inertial, viscous and interfacial forces that contribute to the total force magnitude, a third order polynomial was fitted to the data. Since the inertial forces vary as d^3 , and third order polynomial was chosen. The volume (inertial), surface area (viscous and pressure) and edge (interfacial) are plotted with the respective coefficients (figure 3b) to understand the relative contributions from each force on pinning. For smaller droplets, the contribution from volume and area forces are small, and pinning is achieved by the competition between interfacial restoring forces trying to keep the droplet intact and electrical pinning forces as a droplet boundary passes over a steep potential gradient. In the $50\mu\text{m} - 66.7\mu\text{m}$ range, the area forces become large, continuing to dominate beyond this range for all droplets tested, and thus requiring the pinning electric force to increase. In the higher range of droplet diameter, the constant

interfacial forces are relatively small by comparison.

3.2 Droplet Binning

This pinning behavior has rather large implications for design and control of liquid droplet emulsions in microfluidic devices. Droplet control can be further enhanced by extending the simplified pinning demonstration to binning droplets according to their size. Binning refers to a system's ability to automatically sort more than one object by some physical criteria. This is the exact mechanism used in coin sorting devices, where a group of different coins can enter the device and be grouped automatically by type. This is possible because all of the coins, after entering the device, will pass over a series of different sized openings that will only let through coins smaller than the opening. Likewise, in the current microfluidic system, the droplet size was chosen as the physical criterion for binning into different sized branch channels. While a coin's weight is the force that makes coin binning possible, here, the electric force is responsible for droplet binning. The following simulations illustrate how two droplets of different size can be sorted by leveraging the same electric forces responsible for droplet deceleration and pinning.

Droplet binning was simulated using the same material properties listed in table 1. The continuous channel width remained constant at $w_c = 100\mu\text{m}$, but branched off into a $66.7\mu\text{m}$ width channel, followed by a $100\mu\text{m}$ width channel further downstream, both angled at 60° from the downstream horizontal direction. The flow rate was set to obtain a Reynolds number of $Re = 0.1$. The electrical potential boundary conditions were set such that droplets would decelerate and flow into each of the 60° branches. This required the smoothed step in electrical potential to be located at the upstream corner of the upper channel walls where the branches started. Two deionized water droplets of diameters $86\mu\text{m}$ and $125\mu\text{m}$ were allowed to flow in silicone oil. The results of this simulation can be found in figure 4.

When no electric field was applied, both droplets flowed down the continuous channel without entering the branches (left column of images in figure 4), as there is insufficient electric force to cause the droplets to deviate away from the mainstream flow. The electric field with a steep gradient at the corners (right column of images in figure 4), however, produces enough electric force to route each of the droplets into their equivalently sized branches, thus binning them by size. When the electric potential distribution in the corner is too abrupt or severe ($E_0 = V_0/l_e$ too large), the drops will be pinned to the wall due to the insurmountable electric force. If the electric force is too weak, the droplets will continue downstream unaffected (and "unbinned"). Thus, to achieve binning, a very precise balance between the electric and hydrodynamic forces is required. In the two-branch configuration shown in

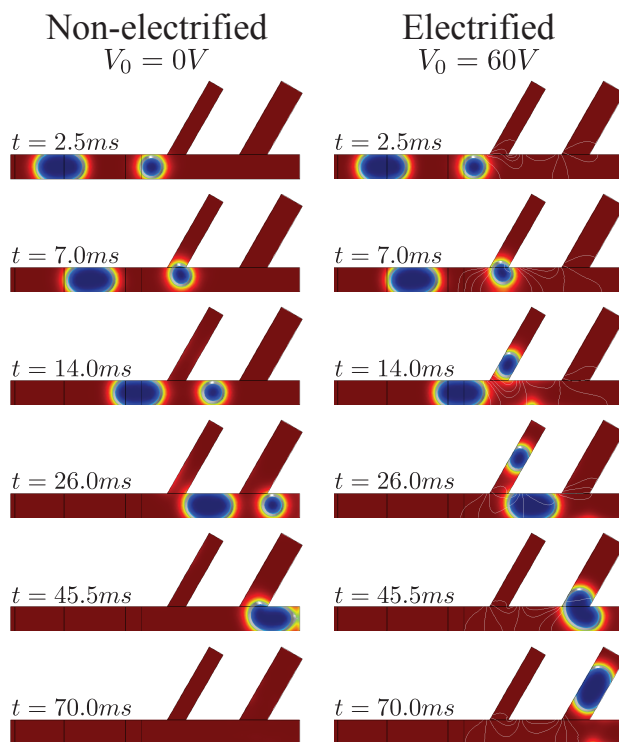


Fig. 4 Three-dimensional simulation of a two droplet binning configuration. Sequence of images are listed for the non-electrified two branch microchannel (left), and the electrified two branch microchannel (right). The white lines in the right column of images are equipotential lines.

figure 4, the first droplet is routed and binned in the first branch due to sufficient electric forces for the given Reynolds number, branch angle (60°) and branch width. When the larger droplet reaches the first branch, the same electric force becomes insufficient for binning due to the increased drop size. However, the same electric force approaching the second branch is sufficient for binning the larger diameter droplet due to the decrease in hydrodynamic forces downstream of the first branch. The hydrodynamic forces decrease downstream of the first branch because the fluid velocity must decrease in order to maintain flow continuity. Table 2 illustrates the dimensionless hydrodynamic to electric force ratios between the two droplet diameters at both the first and second branches.

All of the dimensionless numbers in table 2 contain the hydrodynamic forces in the numerator and the electric forces in their denominator, so a smaller force ratio correlates to a larger electric force (or smaller hydrodynamic force), and vice versa. Since the dielectric force remains constant between the two different diameter droplets, the criterion for routing a droplet into a branch is dependent on the strength of the hydrodynamic

Table 2 List of dimensionless hydrodynamic / electric force ratios for three-dimensional routing simulations, according to equation 9b. N/A values are due to the first droplet being binned at the first branch.

Number	First Branch		Second Branch	
	$d = 86\mu\text{m}$ (binned)	$d = 125\mu\text{m}$ (not binned)	$d = 86\mu\text{m}$ (-)	$d = 125\mu\text{m}$ (binned)
Eu_e	0.073	0.225	N/A	0.092
Ma	27.980	59.111	N/A	37.831
Ps	111.919	236.443	N/A	151.324
Ca_e^{-1}	173.375	251.999	N/A	251.999

forces, which has already been shown to be dependent on the drop size. Approaching the first branch, the force ratios for the second larger droplet are larger than for the first smaller droplet. Therefore, the viscous shear (Ma) and upstream pressure forces (Ps) are able to bin the smaller diameter droplet (smaller Ma and Ps), while allowing the larger droplet to continue downstream (larger Ma and Ps). However, after passing the first branch, the hydrodynamic forces on the larger droplet are reduced due to the decreased flow rate (and average velocity). This is why the same electric force at the second branch is able to bin the large droplet, but was unable to bin it at the first branch. This is also supported by comparing the magnitudes of the force ratios between the $d = 86\mu\text{m}$ droplet at the first branch and the $d = 125\mu\text{m}$ droplet at the second branch.

The force ratio magnitudes for this binning system are also quite large since the system was optimized to find the lowest possible electric force required to bin the droplets. While the force balance does not result in droplet pinning, droplet pinning is not the objective in this system. Rather, it is the delicate balance between a slight deceleration on one side of the droplet and the hydrodynamic pushing of the droplet into a branch, all without pinning the droplet or forcing much larger droplets into the branch. Thus, for an optimized system, the hydrodynamic forces should do most of the work while the electric force simply helps to manipulate droplets in the desired branch.

Additional binning simulations were performed in which the two drop diameters were swept between $d = 75.2\mu\text{m}$ to $d = 167.2\mu\text{m}$. All other parameters (geometric, flow, electrical) were kept identical to the binning simulation outlined earlier. Collecting the terms of equation 9b according to downstream and upstream forces (refer to figure 1), the total dimensionless downstream forces are $F_d = Ma + Ps$ and total dimensionless upstream forces are $F_u = Eu_e + Ca_e^{-1} + 1$. Casting these forces as a ratio (F_d/F_u) gives insight to the relative competition between the upstream and downstream forces on the droplet during the binning simulations, and the subsequent droplet motion. Figure 5 depicts the results of this study.

These binning results follow similar trends to the pinning results covered earlier. One characteristic to note is the sec-

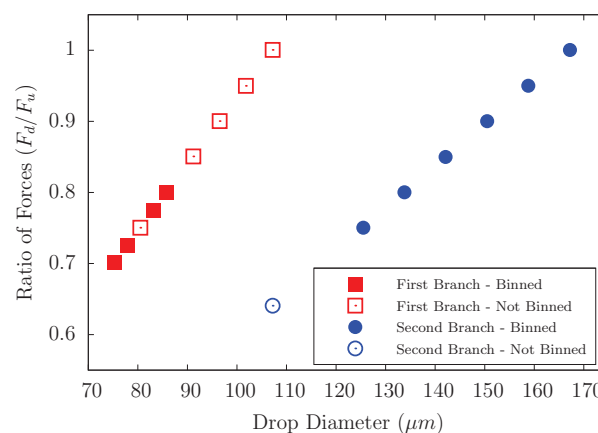


Fig. 5 Three-dimensional simulation of a two droplet binning configuration. Range of drop sizes span $d = 75.2\mu\text{m}$ to $d = 167.2\mu\text{m}$. Filled data points indicate the droplet was binned, and unfilled data points indicate the droplet was not binned.

ond branch requires a much larger drop diameter than the first branch to obtain the same force ratio due to the flow rate reduction after the first branch (smaller Ma and Ps). In addition, a droplet becomes too large to bin in the first (narrower) branch starting around $d = 91\mu\text{m}$, but is still too small to bin in the second (wider) branch. Larger droplets binned very easily in the second branch, even though the droplets were confined and longer than $5w_c$. This behavior is consistent with trends observed in the pinning simulations, where an unconfined droplet requires a higher electric force (i.e. larger voltage) to pin than a droplet whose boundaries are just touching the channel walls (refer to figure 3). As the confined droplet diameter increases further, it again requires more electric force to pin. This illuminates a critical droplet diameter and corresponding minimum pinning electric force for a given microfluidic system. With the pinning simulations, the droplet diameter was increased, and the voltage was adjusted until the droplet pinned to the channel wall. With these binning simulations, all flow, geometric, and electrical parameters were kept constant, and the droplet diameter was the only value ad-

justed. It is analogous to taking a horizontal slice of figure 3, fixing the electric force and sweeping the droplet diameter, monitoring if the droplet pins (or bins, in this case). However, complete mapping of the system depends on where the horizontal “electric forces slice” is taken, and which droplet diameters are simulated, as key features may be missed if the electric force is set to an extreme value. The results shown in figure 5 are more comprehensive since they also monitor the changes in inertial, viscous, pressure, and interfacial forces on the droplet as it changes size, in addition to the electric force.

There are two items in figure 5 that require further investigation. The first is that for $d = 80.5\mu\text{m}$ at the first branch, the droplet does not bin while the drop sizes just smaller and larger than this size do bin. This result suggests a local maximum in the electric force required to bin this particular drop size, and may indicate a geometric effect (such as the branch width and/or angle) that is not yet accounted for in the order of magnitude analysis is playing a larger role than we expected. The second item is that the prevention of binning could not be achieved by further increasing the drop size for the second branch. In the pinning simulations and the binning simulations at the first branch, the droplet could always be increased in size to prevent pinning/binning for a given electrical force. For the second branch binning simulations, even when the confined droplet length achieved $\approx 5w_c$, and the downstream forces were approximately equivalent to the upstream forces, the droplet was still binned. The second branch width was set to match the continuous channel width (w_c), so this again could be a geometric effect that requires further investigation.

4 Conclusions

A three-dimensional numerical study was conducted on droplet motion in the presence of an electric field in a microchannel. Droplet deformation, squeezing, deceleration and pinning were observed in the simulation, and was also qualitatively verified by experiments. The required voltage in the experiment to achieve the same result was larger due to significant attenuation by the bulk PDMS. However, despite any quantitative discrepancies between experiments and numerical simulations in electrode placement, applied voltage and drop size, electrically induced deceleration, squeezing, pinning and release of the droplet is evident. An order of magnitude force balance is presented that describes the electric force necessary to decelerate and pin droplets in continuous microchannel flow, which is consistent with a third order polynomial dependency on the drop diameter.

The angle between each of the branches and the continuous channel, as well as the branch widths, influence the balance between forces during droplet binning. If a branch width is much larger than a droplet, the droplet will naturally flow into the branch when no electric force is applied. This scenario

may allow for another type of passive binning to occur, but this system would need to be much more constrained since only hydrodynamic forces are present (no external forces). Electric fields offer a non-intrusive method binning droplets that can be manipulated without drastically affecting the hydrodynamics of the system. This simplified two drop case demonstrates that droplet binning by size can be conducted passively and on demand for a given combination of electrical, flow, and geometric parameters. In future work, these effects can be coupled with droplet-based mixing via electrocoalescence to enhance the capabilities of the electrohydrodynamic system^{27,28}.

This work is intended to be a foundational study investigating all forces present in a flowing liquid droplet emulsion electrohydrodynamic system. We present pinning and binning as potential applications for these types of systems. While we have provided experimental results that support droplet deceleration (and thus pinning) simulations in this work, we hope to produce experiments that support the binning simulations in future works. Prior to developing the binning experiments (and as a method for refining the device design), we plan on determining a more precise potential distribution along the experimental microchannel boundaries using simulations. This will aid in quantitatively matching pinning simulations with experiments, as well as definitively determine which model to use for mapping the potential distribution through the bulk PDMS.

5 Acknowledgments

The authors acknowledge the University of Central Florida Stokes Advanced Research Computing Center for providing computational resources and support that have contributed to results reported herein. URL: <http://webstokes.ist.ucf.edu>

References

- 1 R. S. Allan and S. G. Mason, *Proceedings of the Royal Society of London: Series A*, 1962, **267**, 45–61.
- 2 S. G. Taylor, *Proceedings of the Royal Society of London: Series A*, 1964, **280**, 383–397.
- 3 J. R. Melcher and G. I. Taylor, *Annual Review of Fluid Mechanics*, 1969, **1**, 111–146.
- 4 D. A. Saville, *Annual Review of Fluid Mechanics*, 1997, **29**, 27–64.
- 5 S. Torza, R. G. Cox and S. G. Mason, *Philosophical Transactions of the Royal Society of London: Series A*, 1971, **269**, 295–319.
- 6 O. Vizika and D. A. Saville, *Journal of Fluid Mechanics*, 1992, **239**, 1–21.
- 7 J. D. Sherwood, *Journal of Fluid Mechanics*, 1988, **188**, 133–146.
- 8 J. Q. Feng and T. C. Scott, *Journal of Fluid Mechanics*, 1996, **311**, 289–326.
- 9 J. Zhang and D. Y. Kwok, *Journal of Computational Physics*, 2005, **206**, 150–161.
- 10 J. Hua, L. K. Lim and C.-H. Wang, *Physics of Fluids*, 2008, **20**, 113302.
- 11 M. N. Reddy and A. Esmaeeli, *International Journal of Multiphase Flow*, 2009, **35**, 1051–1065.

- 12 J. M. Lopez-Herrera, S. Popinet and M. A. Herrada, *Journal of Computational Physics*, 2011, **230**, 1939–1955.
- 13 Y. Lin, *Electrophoresis*, 2013, **34**, 1–9.
- 14 M. Sato, S. Kato and M. Saito, *IEEE Transactions on Industry Applications*, 1996, **32**, 138–145.
- 15 A. Fernandez and G. Tryggvason, *Physics of Fluids*, 2005, **17**, 093302.
- 16 P. Singh and N. Aubry, *Electrophoresis*, 2007, **28**, 644–657.
- 17 T. Krupenkin and J. A. Taylor, *Nature Communications*, 2011, **2**, 448.
- 18 A. R. Abate, T. Hung, P. Mary, J. J. Agresti and D. A. Weitz, *Proceedings of the National Academy of Sciences*, 2010, **107**, 19163–19166.
- 19 J. J. Agresti, E. Antipov, A. R. Abate, K. Ahn, A. C. Rowat, J.-C. Baret, M. Marquez, A. M. Klibanov, A. D. Griffiths and D. A. Weitz, *Proceedings of the National Academy of Sciences*, 2010, **9**, 4004–4009.
- 20 T. Mochizuki, *Langmuir*, 2013, **29**, 12879–12890.
- 21 M. W. Lee, S. S. Latthe, A. L. Yarin and S. S. Yoon, *Langmuir*, 2013, **29**, 7758–7767.
- 22 S. J. Lee, J. Hong, K. H. Kang, I. S. Kang and S. J. Lee, *Langmuir*, 2014, **30**, 1805–1811.
- 23 J. Hong, Y. K. Kim, K. H. Kang, J. M. Oh and I. S. Kang, *Langmuir*, 2013, **29**, 9118–9125.
- 24 J. D. Wehking, L. Chew and R. Kumar, *Applied Physics Letters*, 2013, **103**, 054101.
- 25 E. Olsson, G. Kreiss and S. Zahedi, *Journal of Computational Physics*, 2007, **225**, 785–807.
- 26 A. C. Siegel, D. A. Bruzewicz, D. B. Weibel and G. M. Whitesides, *Advanced Materials*, 2007, **19**, 727–733.
- 27 M. Zagnoni and J. M. Cooper, *Lab on a Chip*, 2009, **9**, 2652–2658.
- 28 M. Zagnoni, G. Le Lain and J. M. Cooper, *Langmuir*, 2010, **26**, 14443–14449.